Applied Physics A (2024) 130:387
https://doi.org/10.1007/s00339-024-07495-7

Applied Physics A
Materials Science & Processing

Double hysteresis (P-E) loops in the transparent composite containing $BaTiO_3$ at room temperature

E. K. Abdel-Khalek[1] · E. A. Mohamed[2] · Yasser A. M. Ismail[3]

Received: 15 January 2024 / Accepted: 1 April 2024

Abstract
A transparent composite sample containing $BaTiO_3$ was synthesized by using the melting quenching method. The presence of a glassy phase in this composite sample was detected through XRD analysis, and this was further confirmed by DSC study. TEM and SAED analyses provided evidence that the $BaTiO_3$ nanoparticles/clusters are embedded within the borate glass matrix, establishing the composite nature of this sample. FTIR spectrum of the present sample revealed that the glass matrix is composed of two structural groups (BO_3 with NBO's, and BO_4), along with the distinct groups for $BaTiO_3$. XPS spectra of the present composite sample indicated the presence of more than one type of boron, barium, titanium and oxygen. DSC and dielectric studies of the present composite sample revealed the presence of the phase transition temperature (T_c). Dielectric constant (ε_r) and dielectric loss (tan δ) curves of the present composite sample displayed an anomaly peak in the vicinity of T_C. The optical transmission spectrum of the present composite sample exhibit two transmission bands of Ti^{3+} ($3d^1$) ions in tetragonal distorted sites. At room temperature, the present transparent composite sample exhibited double hysteresis loops for $BaTiO_3$ at low electric fields. The results obtained can be used for the development of lead-free ferroelectric material.

Keywords Transparent composite · Double hysteresis loops · Thermal · Dielectric · Optical properties

1 Introduction

Recently, transparent composite containing $BaTiO_3$ have attracted much attention because of their promising applications in electronic and optoelectronic devices [1–4]. These composite materials exhibit promising characteristics which due to the presence of two constituents namely the $BaTiO_3$ nanoparticles and the glass matrix [2, 3]. The change of the ferroelectric behavior of ABO_3 (such as $SrTiO_3$ and $BaTiO_3$) in the amorphous matrix or glass matrix arises from the strain induced during the growth of nanoparticles within the host matrix [5, 6]. This strain within the amorphous matrix or glass matrix causes the TiO_6 octahedra to rotate in opposite directions concerning their neighboring octahedra [7]. With the ongoing trend towards the miniaturization of electronic devices, the reduction of the particle size of ferroelectric materials embedded in a glass matrix has a significant impact on their polarization and phase transition temperatures [5, 6]. $BaTiO_3$ is one of the foremost ferroelectric materials because of its technological importance. When $BaTiO_3$ nanoparticles embedded in the glass matrix, they give unconventional properties [1, 4]. Merz reported that the double hysteresis loop (P-E) for $BaTiO_3$ was observed near Curie temperature as well as the shape and the size of these loops was changed with increasing the temperature [8]. The double hysteresis loop (P-E) can result from antiferroelectric materials, electric field induced near Curie temperature, and/or aging effect below Curie temperature [9]. In the case of aged Mn-doped $BaTiO_3$ single crystal, the double hysteresis loop (P-E) arises due to recoverable electro-strain [10, 11]. Shebanov et al. reported that the transition between antiferroelectric and ferroelectric phases can be induced by electric field, temperature variation, or mechanical stress [12].

Among various host matrices, borate glasses (B_2O_3) have been widely used because of their advantageous properties

✉ E. K. Abdel-Khalek
eid_khalaf1@yahoo.com; eid_khalaf1@azhar.edu.eg

✉ Yasser A. M. Ismail
Yasser_ami@yahoo.com

[1] Department of Physics, Faculty of Science, Al-Azhar University, Cairo, Nasr City 11884, Egypt

[2] Department of Physics, Faculty of Science (Girl's Branch), Al-Azhar University, Cairo, Nasr City 11884, Egypt

[3] Department of Physics, Faculty of Science, Islamic University of Madinah, Medina, Saudi Arabia

Published online: 09 May 2024

such as good glass forming ability, low melting point, high transparency, high thermal stability, as well as have a large variety of structural units (diborate, triborate, and tetraborate) [1, 13]. Therefore, the solubility of the $BaTiO_3$ ferroelectric nanoparticles in borate glasses is high [14]. Abdel-Khalek et al. investigated the $(100–x)Li_2B_4O_7–xBaTiO_3$ (where x = 0, 20, and 60 mol%) and $(30–x)V_2O_5–xBaTiO_3 – 70TeO_2$ (where x = 5, 10, and 15 mol%) systems and they found that the $BaTiO_3$ ferroelectric nanoparticles are formed within glass matrices during the glass formation via the melt-quenching method [1, 3]. Furthermore, the ferroelectric-paraelectric transition temperature (T_C) of $BaTiO_3$ nanoparticles in glass matrix was identified through dielectric studies. Singh et al. investigated the addition of $BaTiO_3$ into bismuth borate glasses containing $1Dy_2O_3$ and observed the gradual conversion of BO_3 into BO_4 units, along with a decrease in the optical band gap energy as the $BaTiO_3$ content increased [4]. Despite numerous studies on composites containing $BaTiO_3$ ferroelectric nanoparticles, there has been notable absence of investigation regarding the polarization-electric field (P-E) characteristics of the $BaTiO_3$ nanoparticles embedded in a borate glass matrix. It is well known that P-E loop is used to characterize a ferroelectric material which is considered as the fingerprint for the information on the structure and properties of this material [15]. In the present investigation, we have fabricated $BaTiO_3$ nanoparticles embedded in borate glass matrix with the composition 25 $BaTiO_3$– 75 B_2O_3 (in mol %). The structural, thermal, optical, and P-E properties of this sample have been investigated.

2 Experimental procedures

A transparent composite sample with the composition of 25 $BaTiO_3$– 75 B_2O_3 (in mol %) was prepared by using the melting quenching method. The raw materials employed in the preparation of this composite were high-purity B_2O_3 (99.99%), and $BaTiO_3$ (99.99%). These raw materials were initially ground in an agate mortar and subsequently melted in a porcelain crucible at a temperature of 1150 °C for one hour using an electric furnace. The resultant molten materials were expeditiously poured and quenched onto a copper plate and immediately pressed into plates at room temperature to obtain this composite sample. X-ray diffraction (XRD) pattern of the present transparent composite sample was carried out using a Bruker Co D8 Discover X-ray diffractometer with Cu Kα radiation of wavelength 1.54 Å operating at 40 kV and 40 mA. The transmission electron microscopy (TEM), selected area electron diffraction (SAED), and high-resolution transmission electron microscopy (HR-TEM) studies of the present transparent composite sample were carried out using a JEOL model JEM-2100 PLUS with LaB6 source operating at an accelerating voltage of 200 kV. The energy dispersive X-ray spectroscopy (EDS) elemental mapping analysis of the present transparent composite sample were performed on a JEM-2100 F (URP) instrument operating at 200 kV and equipped with Dry SD30GV Detector. Fourier transform infrared (FTIR) spectrum of the present transparent composite sample was recorded using a Thermo Scientific Nicolet iS50 FT-IR spectrometer with KBr pellets. The FTIR spectrum data were collected in the wavenumber range of 400–1800 cm^{-1}, with a spectral resolution of 4 cm^{-1} at room temperature. X-ray photoelectron spectroscopy (XPS) of the present transparent composite sample was carried out using a Thermo Scientific™ K-Alpha™ USA with a monochromatic AL-K_α radiation source. Differential scanning calorimetry (DSC) of the present transparent composite sample was carried out using a TA Instrument STA model 650 in the temperature range from 30 to 1100 °C at a heating rate of 15 °C/min. The dielectric constant (ε_r) and dielectric loss (tan δ) as a function of temperature at different frequencies ranging from 1 to 100 kHz for the present composite sample was measured by using an electronic RLC bridge type SR 720. Optical transmission spectrum of the present transparent composite sample, in the wavelength range 190–824 nm, was carried out using a Hitachi 6405 spectrophotometer. The polarization-field (P-E) loops at various electric field of the present transparent composite sample were recorded at room temperature. This measurement was carried out using a ferroelectric tester (Precision premier II, Radiant technologies Inc., USA) at a frequency of 10 Hz.

3 Results and discussion

3.1 XRD, TEM, SAED, and HR-TEM studies

Figure 1 displays the XRD pattern of the present transparent composite sample at room temperature. This pattern is characterized by broad humps without any distinct sharp Bragg peaks for crystalline $BaTiO_3$. This feature suggests the presence of amorphous nature (glassy phase) of the present transparent composite sample. The present XRD pattern fails to reveal the crystallinity of the $BaTiO_3$ nanoparticles within the borate glass matrix, mainly due to their small size and low concentration in glass matrix [1, 16]. Figure 2 displays the photograph of the present transparent composite sample. It is noticed that the present sample exhibits transparency and appears yellow when observed at a macroscopic level. This observation provides evidence of the presence of a small amount of Ti^{3+} in the present sample thus evidence of the incorporation of $BaTiO_3$ nanoparticles within the borate glass matrix [1, 16].

Figure 3a displays the TEM image of the present transparent composite sample, captured in the first selected region.

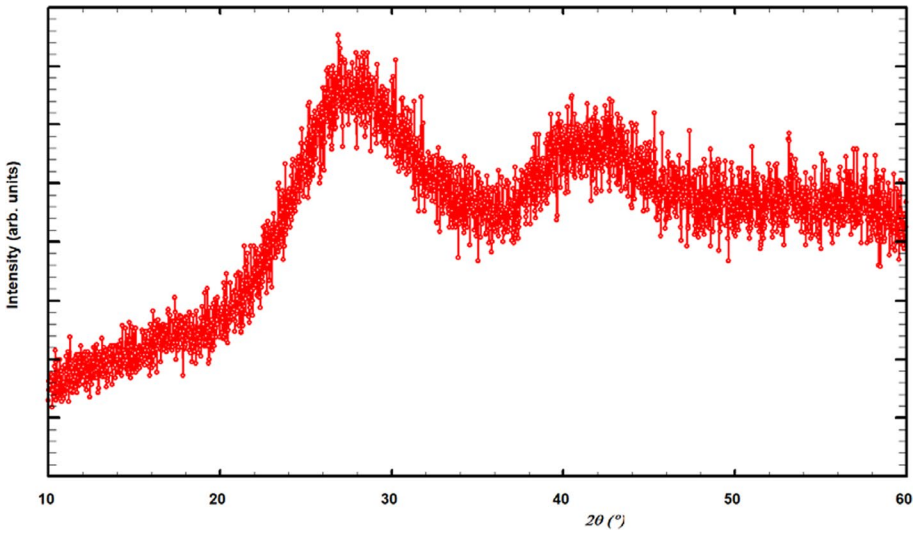

Fig. 1 XRD pattern of the present transparent composite sample at room temperature

Fig. 2 The photograph of the present transparent composite sample

This image clearly displays the $BaTiO_3$ nanoparticles/clusters phase (dark) embedded within a continuous borate glass matrix phase (gray region). This observation leads to the conclusion that the present sample is indeed a glass-nanocomposite, characterized by the presence of two different constituents namely the $BaTiO_3$ nanocrystalline phase and glass matrix. This finding aligns with reported for (100–x) $Li_2B_4O_7$–x$BaTiO_3$ (where x = 20, and 60 mol%) glass-nanocomposite by Abdel-Khalek et al. [1, 16]. Figure 3b displays the SAED pattern of the present transparent composite sample obtained from Fig. 3a. The SAED pattern consists of diffuse rings or halos, indicating the presence of an amorphous nature (glassy phase) in this sample [17]. Figure 3c displays another TEM image of the present transparent composite sample, captured in the second selected region. Like the previous TEM image, it clearly displays the presence of $BaTiO_3$ nanoparticles phase (dark) embedded within the continuous borate glass matrix (gray region). Figure 3d displays the SAED pattern of the present transparent composite sample obtained from Fig. 3c. This pattern exhibits diffraction rings with some spots surrounding the bright central region. These diffraction rings confirm the presence of $BaTiO_3$ polycrystalline structure [18]. Therefore, it becomes evident from the electron diffraction pattern that the present sample is indeed a glass-nanocomposite, given the coexistence of amorphous (borate glass matrix phase) and crystalline ($BaTiO_3$ nanoparticles) states in this sample.

Figure 4 displays the elemental mapping images of the present transparent composite sample. These images display the distribution of barium (Ba), boron (B), oxygen (O), and titanium (Ti) elements. All these elements are uniformly distributed, and no other elements show up (impurities). This observation underscores the purity of the present glass-nanocomposite sample. To identify the shape and determine the average particle size of $BaTiO_3$ nanoparticles/clusters, a specific area containing these nanoparticles/clusters was magnified, as shown in Fig. 5a. The particles of $BaTiO_3$ (Fig. 5a) exhibit a predominantly spherical shape with some slight agglomeration. The distribution of particle size histograms of the $BaTiO_3$ nanoparticles is shown in Fig. 5b. The histogram has been fitted with a Gaussian distribution, which allows us to determine the average particle size of the $BaTiO_3$ particles. The average particle size was found to be 44.489 nm. This finding indicates that the present sample is indeed a glass-nanocomposite natures, where the particle size of $BaTiO_3$ within the borate glass matrix falls within the nanoscale regime. Figure 5c displays the HR-TEM image captured from the region described in Fig. 3c. In this

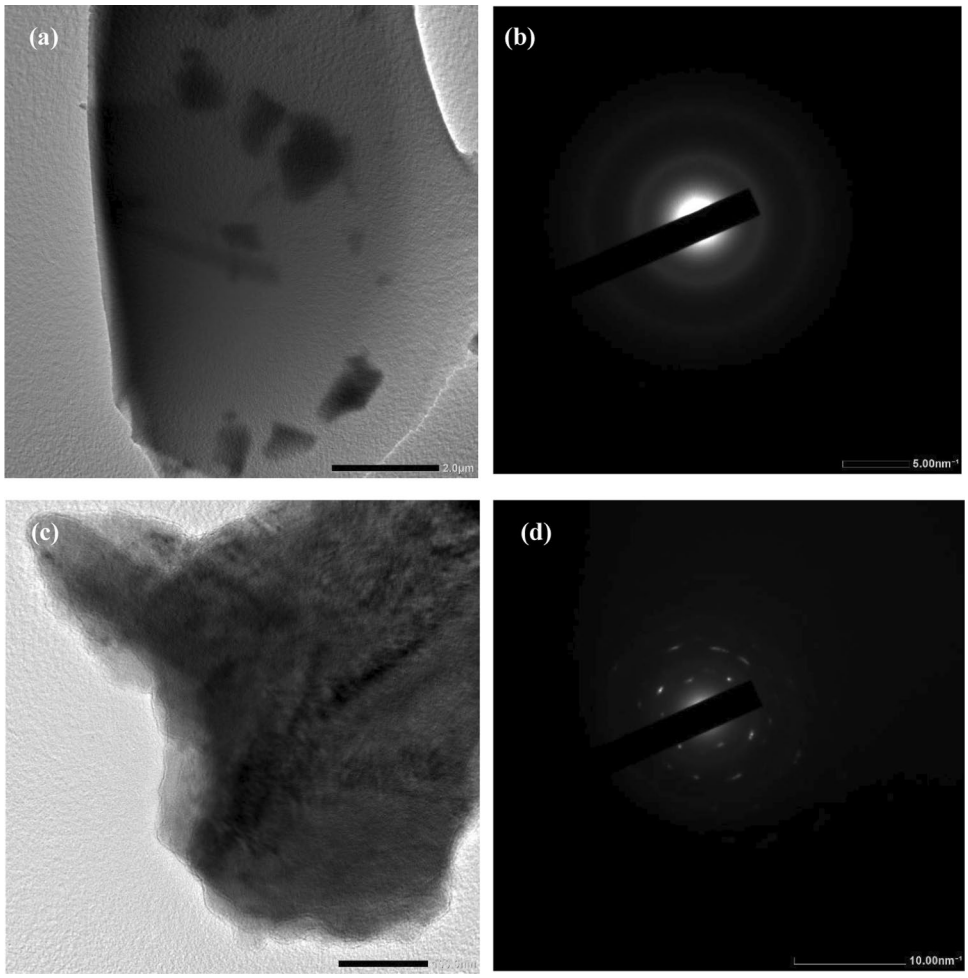

Fig. 3 **a**–**d** The transmission electron microscope (TEM) images along with the selected area electron diffraction (SAED) patterns of the present transparent composite sample at first and second regions, respectively

image, regions with aligned bright planes (lattice fringes), representing the $BaTiO_3$ phase. In contrast, the remaining regions lack these lattice planes (lattice strips), indicating the presence of the borate glass phase [19]. Moreover, the HR-TEM image displays non-uniform lattice fringes with blurry edge, signifying the presence of $BaTiO_3$ nanoparticles within the borate glass matrix [20]. The interplanar spacing (fringes) as estimated from Fig. 5c is approximately 0.34 nm, corresponding to the (100) plane in the tetragonal $BaTiO_3$ structure (JCPDS File No. 812,203) [21, 22]. This observation confirms the presence of tetragonal $BaTiO_3$ in our sample, characterized by high crystallinity of the particles. It's worth noting that the interplanar spacing in our sample is higher than that found in Refs. [21, 22]. Additionally, the $BaTiO_3$ nanoparticles in our sample exhibit the formation of extended defects, marked with green ovals, as shown in Fig. 5c. These extended defects have an influence on the ordering of oxygen vacancies in the $BaTiO_3$ [23]. Figure 5d displays the SAED pattern taken from the region in Fig. 5c. This pattern exhibits clear spots, indicating the presence of the $BaTiO_3$ perovskite structure with high crystallinity. This serves as confirmation of the presence of $BaTiO_3$ nanoparticles in our sample. To determine the elemental composition of the nanoparticles/clusters embedded within the borate glass matrix, elemental mapping images of the $BaTiO_3$ nanoparticles were obtained from the region in Fig. 5a, as shown in Fig. 6. These images reveal the distribution of barium (Ba), titanium (Ti), and oxygen (O) elements. Additionally, these elements are uniformly distributed, and there are no indications of other elements, affirming the presence of $BaTiO_3$ nanoparticles/clusters embedded in the borate glass matrix.

3.2 FTIR and XPS studies

Figure 7a displays the FTIR absorption spectrum of the present transparent composite sample in the wavenumber range of 400–1800 cm^{-1} at room temperature. This spectrum exhibits broad bands, which are a result of the overlapping of the individual bands. To resolve and identify the individual bands that are concealed within the broad spectrum, we deconvoluted the FTIR absorption spectrum of the transparent composite sample based on Gaussian type function as shown in Fig. 7b. This deconvolution revealed twelve distinct

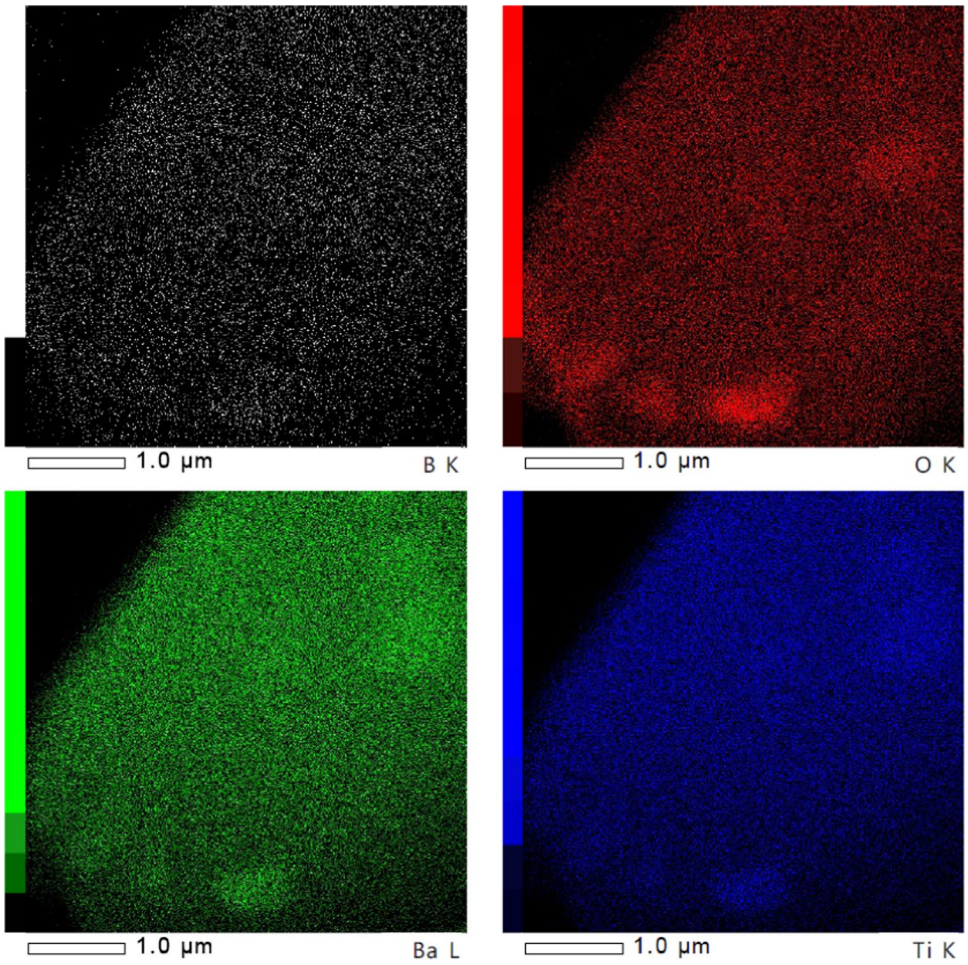

Fig. 4 The elemental mapping images of the present transparent composite sample

bands. The band at 1635 cm^{-1} is assigned to OH bending mode of vibration [23]. The band at 1630 cm^{-1} is assigned to asymmetric stretching relaxation of the B–O bond in trigonal BO_3 units [24]. The band at 1504 cm^{-1} is attributed to the B–O asymmetric stretching vibration of BO_3 units in pyro-borate and ortho-borate groups [25]. The band at 1466 cm^{-1} is due to the asymmetric vibrations mode involving three non-bridging oxygen (NBOs) in the B–O–B groups [24, 26]. The band at 1401 cm^{-1} corresponds to the stretching vibration of various network containing six-membered borate groups in BO_3 units [23]. The band at 1284 cm^{-1} is assigned to the B–O–B bond that links neighboring groups to boroxol groups [23, 27]. The band at 1098 cm^{-1} results from the stretching vibration of BO_4 units, including triborate, tetraborate, and pentaborate groups [28]. The band at 1033 cm^{-1} can be attributed to the B–O stretching vibration of BO_4 groups in diborate groups [29]. The band at 916 cm^{-1} is assigned to the stretching vibration of tetrahedral BO_4 units [14]. The band at 693 cm^{-1} is assigned to the bending vibrations of B–O–B linkages in the borate network or may be assigned to the stretching vibrations of Ti–O bonds in octahedral TiO_6 units [3]. This band indicates the presence of Ti^{4+} at octahedral sites in the glass network [1, 30]. The band at 569 cm^{-1} results from the TiO_6 octahedra deformation mode of $BaTiO_3$ [1]. Finally, the band at 465 cm^{-1} is attributed to vibrations of Ba^{2+} metallic cations in $BaTiO_3$ [30]. The presence of this band in the present composite sample may be due to Ti^{3+} ions in tetragonally distorted octahedral sites, as further confirmed by subsequent optical results [31]. These FTIR results validate the presence of the ferroelectric $BaTiO_3$ nanoparticles phase embedded within the borate glass matrix. Furthermore, the borate glass matrix is composed of the network former BO_3 with non-bridging oxygen (NBO's), and BO_4 within the glass network.

Figure 8a–d displays XPS spectra of the B 1s, Ba 3d, Ti 2p, and O 1s core levels of the present transparent composite sample. These spectra confirm the present composite sample is composed of the expected species, namely B, Ba, Ti, and O. The B 1s XPS spectrum of the present transparent composite sample is shown in Fig. 8a. Deconvolution of the B 1s XPS spectrum revealed two individual peaks at 189.71 and 192.55 eV, corresponding to the boron species present [32]. This spectrum closely resembles those previously reported for borate glasses [32, 33]. The B 1s peak at lower binding

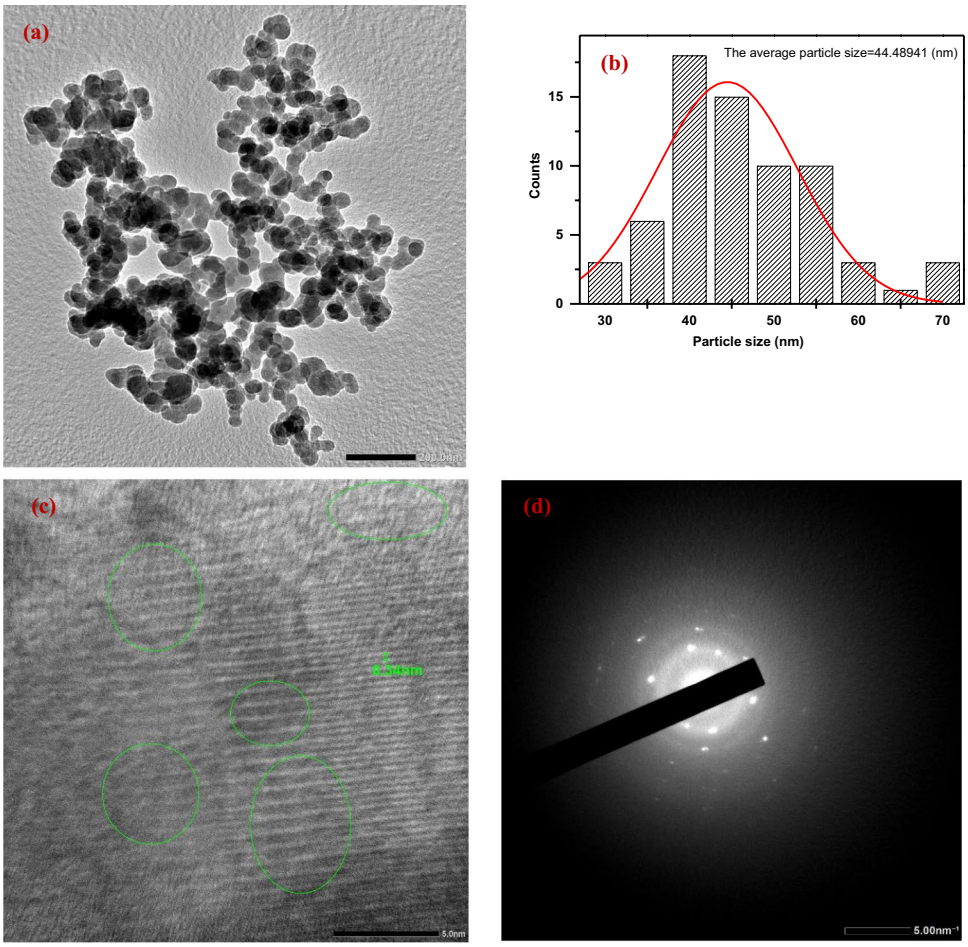

Fig. 5 **a**–**d** The shape of the particle of $BaTiO_3$ nanoparticles/clusters in the present transparent composite sample, the distribution of particle size histogram, and the HR-TEM image taken from the region in Fig. 3c, and the SAED pattern taken from the region in Fig. 5c, respectively

energy of 189.71 eV is due to the formation of boron with nonbridging oxygen (NBO) in the present sample [33]. The B 1s peak at higher binding energy of 192.55 eV arises from the formation of B_2O_3 with bridging oxygen (BO) in the present sample [33]. Figure 8b displays the Ba 3d XPS spectrum of the present transparent composite sample, revealing two peaks of $3d_{5/2}$ and $3d_{3/2}$ at 780.58 and 795.88 eV, respectively. This spectrum closely resembles that reported by Harizanova et al. for strontium barium titanate glass-ceramics [34]. The peak at a binding energy of 780.58 eV, corresponding to $3d_{5/2}$ is attributed to Ba^{2+} ions within the $BaTiO_3$ lattice [35]. The other peak at a binding energy of 795.88 eV, corresponding to $3d_{3/2}$ is assigned to Ba^{2+} ions located at the surface region of $BaTiO_3$ [36]. The Ti 2p XPS spectrum of the present transparent composite sample is shown in Fig. 8c. This spectrum reveals four individua peaks of 2p3/2 and 2p1/2, indicating the presence of different oxidation states of Ti ions [34]. The peaks at binding energies of 459.01 and 461.63 eV correspond to $2p_{3/2}$ and $2p_{1/2}$ respectively. Additionally, the peaks at binding energies of 464.69 and 472.63 eV also correspond to $2p_{3/2}$ and $2p_{1/2}$ respectively. The peaks at higher binding energies are attributed to the existence of Ti^{4+} ions, while those at lower binding energies may be attributed to the presence of Ti^{3+} ions [34]. The O 1s XPS spectrum of the present transparent composite sample is shown in Fig. 8d. The XPS spectrum of O 1s for the present sample could be deconvoluted into two individual peaks, consistent with previous literature [35, 37]. According to Gong et al. the O 1s XPS spectrum of 7 wt% glass-$BaTiO_3$ exhibits two peaks attributed to bridging oxygen (BO) and nonbridging oxygen (NBO) [35]. The O 1s peak at a binding energy of 531.74 eV corresponds to oxygen in the $BaTiO_3$ lattice [37, 38]. Meanwhile, the O 1s peak at a binding energy of 534.56 eV is attributed to O^{2-} ions originating from oxygen vacancies [36]. The presence of oxygen vacancies in the present transparent composite sample contributes to the existence of Ti^{3+} ions [38, 39].

3.3 Thermal and dielectric studies

Figure 9 displays the DSC curve of the present transparent composite sample at the heating rate of 15 °C/min. At approximately 30 °C, an endothermic peak is observed, followed by an endothermic dep at 588 °C. These endothermic features represent the Curie temperature (T_c) of the $BaTiO_3$ (ferroelectric to paraelectric) and the glass transition

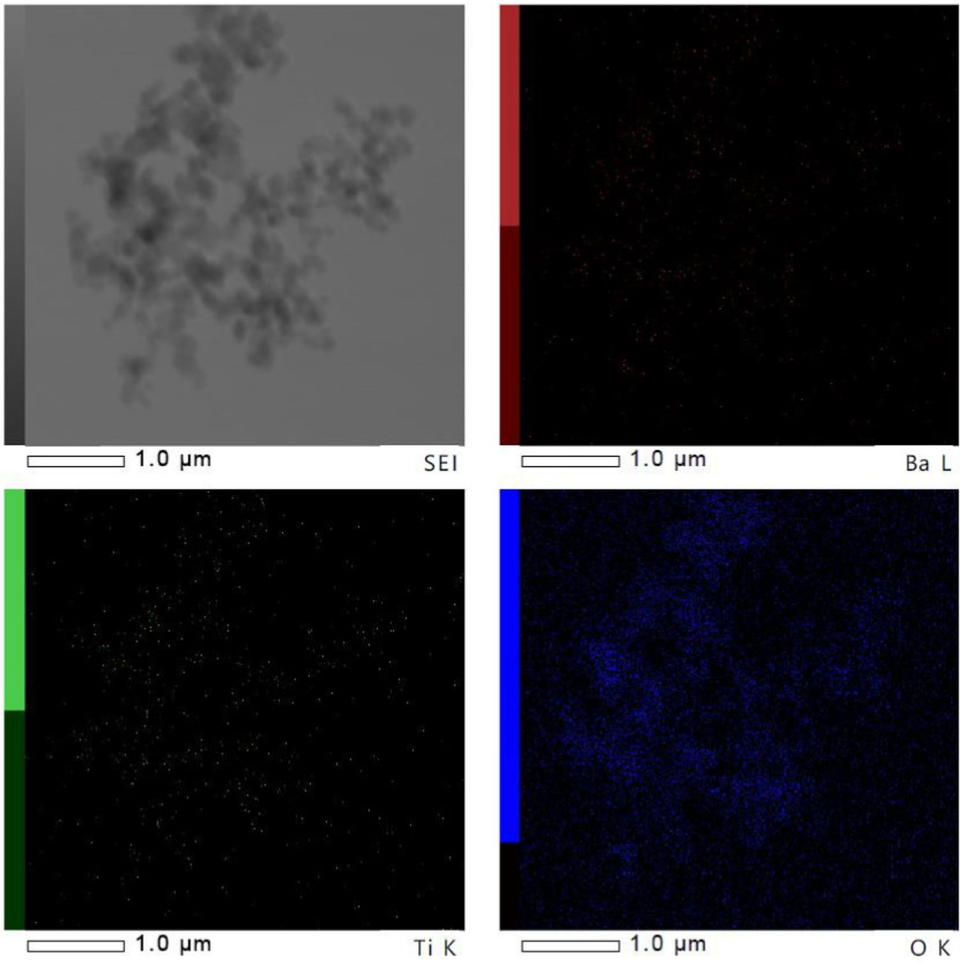

Fig. 6 The elemental mapping images of the $BaTiO_3$ nanoparticles/clusters in the present transparent composite sample

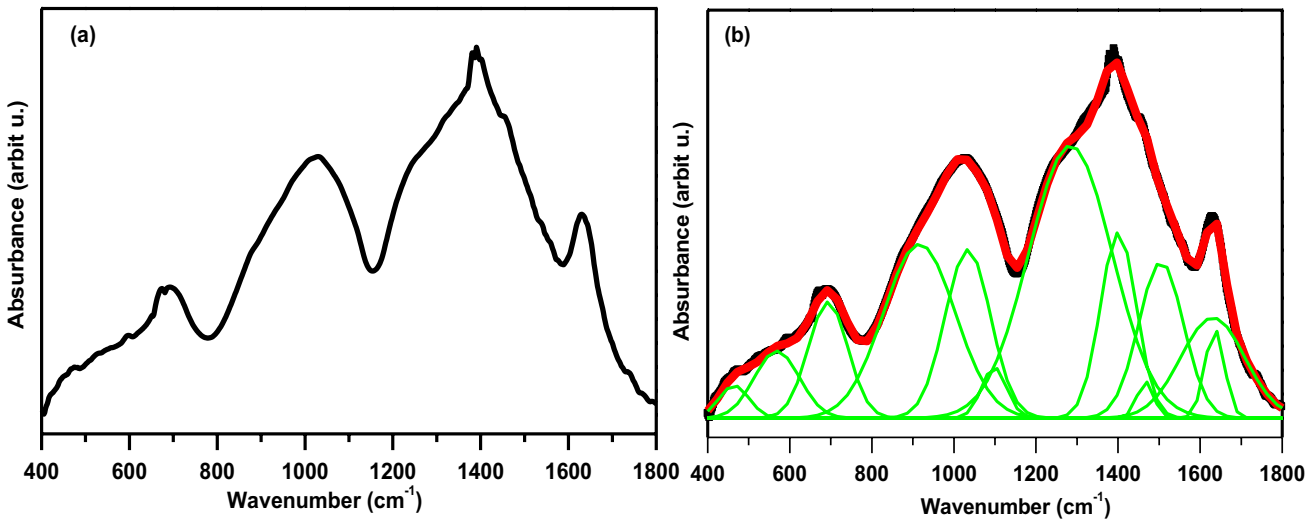

Fig. 7 **a** and **b** The FTIR absorption spectrum and its deconvolution, in Gaussian bands, for the present transparent composite sample, respectively

temperature (T_g) respectively [16]. This observation confirms the presence of ferroelectric $BaTiO_3$ nanoparticles within the borate glass matrix, defining it as a glass-nanocomposite [1, 16]. Additionally, the DSC curve further

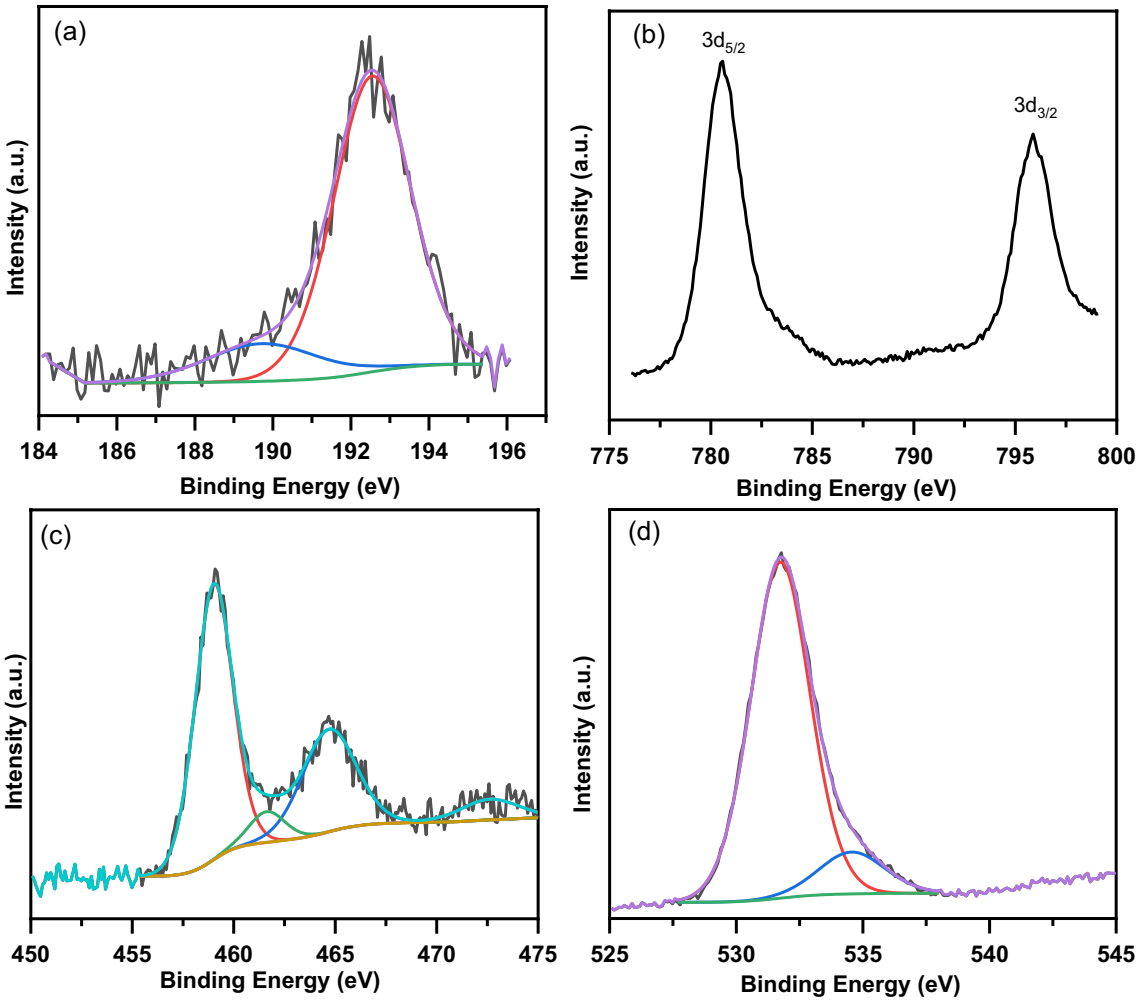

Fig. 8 **a–d** The XPS spectra of the B 1s, Ba 3d, Ti 2p, and O 1s core levels of the present transparent composite sample

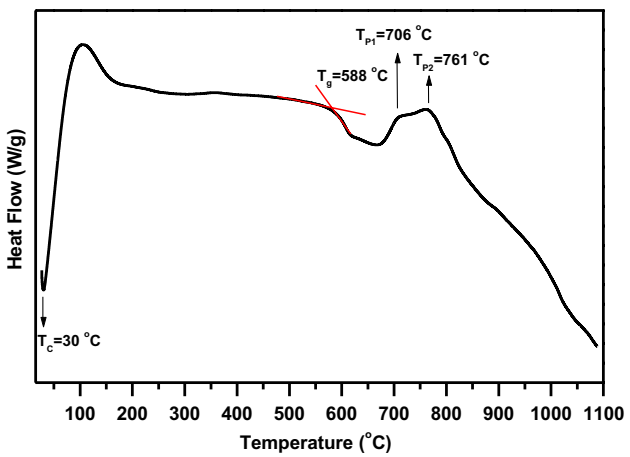

Fig. 9 The DSC curve of the present transparent composite sample at heating rate 15 °C/min

exhibits two exothermic peaks at T_{P1}=706 (less intense) and T_{P2}=761 °C (more intense). These exothermic peaks represent the crystallization process. The presence of two distinct exothermic peaks suggests the crystallization of two different phases [26]. Moreover, the differing intensities of these peaks imply that one of the two mechanisms, either nucleation or growth, dominates the crystallization process [26]. The large difference between T_g and the onset T_p underscores the thermal stability of the present transparent composite material, highlighting its suitability for various applications. The DSC results align well with the observations made through TEM, SAED, and FTIR analyses, collectively confirming the composite nature of the material.

Figure 10 displays the dielectric constant (ε_r) as a function of temperature at different frequencies in 1–100 kHz range for the present transparent composite sample. It is observed that the values of ε_r are larger at higher temperatures and lower frequencies, indicating the wide range of applications for the present composite [14]. The increase

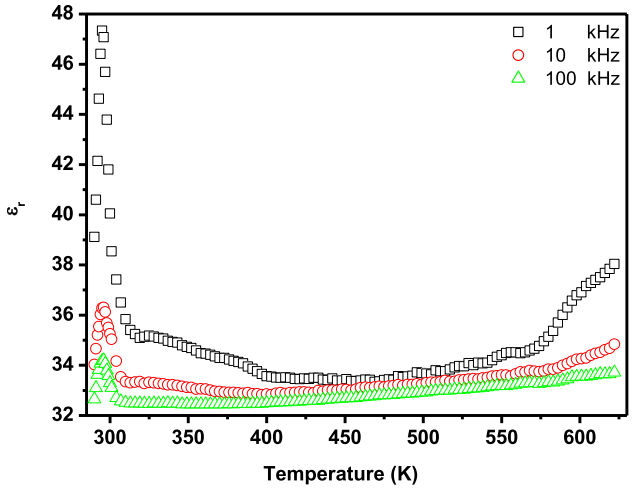

Fig. 10 The ε_r as a function of temperature at different frequencies in 1–100 kHz range for the present transparent composite sample

in ε_r values with increasing temperature is due to the increase in both electronic and ionic polarizability sources [1]. The decrease in ε_r values with increasing frequency is attributed to the decrease in orientation and ionic polarizability sources [1]. Furthermore, the increase in ε_r values at higher temperatures and lower frequencies may be due to the increase in space charge polarization near the interface between $BaTiO_3$ nancrystallites and the glass matrix [40, 41]. Additionally, the ε_r curves at all studied frequencies display an anomaly peak, attributed to the phase transition temperature (T_c) of the $BaTiO_3$ phase, consistent with DSC results [1]. Figure 11a displays the ε_r as a function of temperature at 1 kHz for the anomaly peak. It is apparent from Fig. 11a that the T_c of $BaTiO_3$ phase is 295 K. The values of T_C of $BaTiO_3$ phase in the present composite sample closely align with those reported by Abdel-Khalek et al. [1, 16]. The broad of the anomaly peak may be due to presence of both non-homogeneous and internal stresses in the present composite [1]. According to Xiao et al. the polycrystalline $BaTiO_3$ have phase transition temperatures, are 1432, 130, 5, – 90 °C, corresponding to the transition between hexagonal, cubic, tetragonal, orthorhombic and rhombohedral, respectively [42]. Amongst them, the tetragonal phase (P4mm) is stable at room temperature [42]. This result is consistent with the XRD pattern of the $BaTiO_3$ raw material used in the preparation of the present composite as shown in Ref. [43]. The change in the T_c value of in present composite may be attributed to the lower particle size of $BaTiO_3$ (44.489 nm). In addition, the presence of the strained $BaTiO_3$ nanoparticles because of borate glass matrix [6].

To determine the order of the phase transition, the relationship between the reciprocal of dielectric constant ($1/\varepsilon_r$) and the temperature above T_c follows the Curie-Weiss law.

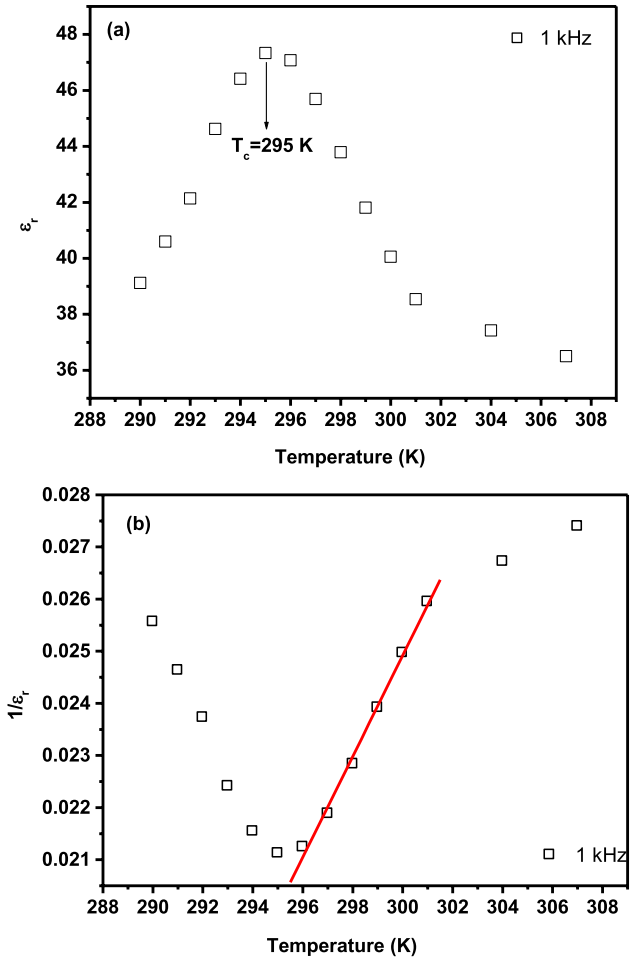

Fig. 11 **a** and **b** The ε_r and $1/\varepsilon_r$ as a function of temperature at 1 kHz for the anomaly peak, respectively

$$\varepsilon_r = C/(T - T_0), \tag{1}$$

where C represents the Curie-Weiss constant and T_0 signifies the Curie-Weiss temperature. Figure 11b displays the $1/\varepsilon_r$ as a function of temperature at 1 kHz for the present transparent composite sample. From the linear fitting, the values of C, T_0 and the difference (T_c– T_0) for the present composite sample are determined to be 1.034×10^3, 274 K, and 21 K, respectively. The magnitude of C and T_0 closely match the values obtained in the previous studies of $BaTiO_3$ in glass-nanocomposite samples [2, 16]. The fact that the difference (T_c– T_0) is larger than zero, indicates that the phase transition in the present composite sample is of the first order [2, 16]. Figure 12 displays the dielectric loss (tan δ) as a function of temperature at different frequencies ranging from 1 to 100 kHz for the present transparent composite sample. It is observed that the behavior of tan δ, exhibiting larger values at both higher temperatures and lower frequencies, is similar to that for the dielectric constant. Moreover, the tan δ curves at all studied frequencies display an anomaly peak

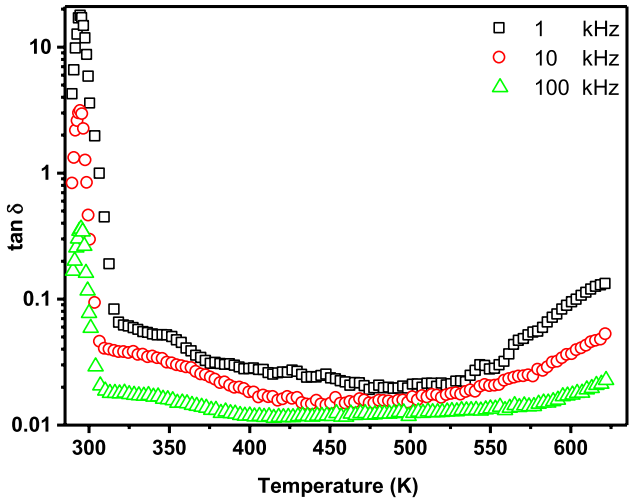

Fig. 12 The tan δ as a function of temperature at different frequencies ranging from 1 to 100 kHz for the present transparent composite sample

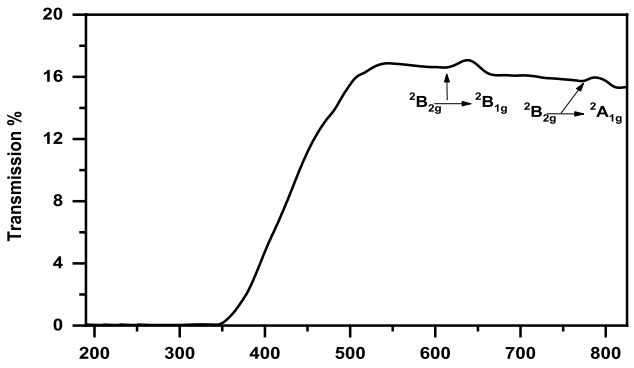

Fig. 13 The optical transmission spectrum of the present transparent composite sample at room temperature

in the vicinity of T_C. The high value of tan δ at T_C can be attributed to the coupling between space charge and ferroelectricity [44]. The presence of space charge in the present composite sample is attributed to the oxygen vacancies in $BaTiO_3$ nanoparticles, contributing to electrical polarization [44]. Beyond T_C, the tan δ values decreases with increasing temperature up to approximately 475 K. This decrease can be attributed to the decreasing contribution of ferroelectric domain walls [41]. However, as the temperature rises above 475 K, conduction loss increases while relaxation loss diminishes [3, 23]. At lower frequencies, the higher values of tan δ may be due to the contribution of conduction loss and electron polarization loss while the decrease in tan δ values with increasing frequency may be attributed to electron polarization loss [23].

3.4 Optical and ferroelectric studies

Figure 13 displays the optical transmission spectrum of the present transparent composite sample at room temperature in the wavelength range (200–825 nm). This spectrum exhibits relatively low levels of transparency and have two distinct transmission bands at 614 and 773 nm. These bands are assigned to the $^2B_{2g} \rightarrow {}^2B_{1g}$ and $^2B_{2g} \rightarrow {}^2A_{1g}$ octahedral transitions of Ti^{3+} ($3d^1$) ions located in tetragonal distorted sites, respectively [1]. These bands agree with that reported for $40Li_2B_4O_7$–$60BaTiO_3$ (mol%) glass-nanocomposite, $55B_2O_3$–$(25–x)ZnF_2$–$10CaF_2$–$10Al_2O_3$:$xTiO_2$ ($0 \le x \le 1$) mol%, and LiF-PbO-B_2O_3 glasses containing different concentration of TiO_2 by Abdel-Khalek et al. [1], Lakshmi et al. [31], and Rao et al. [45], respectively. A significant observation is the shift of these bands to longer wavelength in the present transparent composite sample. This shift suggests a weaker ligand field of Ti^{3+} ($3d^1$) ions, influencing the optical properties of this material [1]. The optical absorption edge ($\lambda_{cut\text{-}off}$) of the present transparent composite sample equals to 348 nm. To determine the optical band gap (E_{opt}) of the present transparent composite sample, we used the following Mott and Davis relation [46].

$$\alpha(\nu)h\nu = B(h\nu - E_{opt})^2 \quad (2)$$

where B is a constant independent of energy, hν is the incident photon energy and α(ν) is the optical absorption coefficient. Figure 14a shows the $(\alpha\, h\nu)^{1/2}$ versus hν plot for the present transparent composite sample. The plot demonstrates a linear region, and by extrapolating the linear portion to the point where $(\alpha\, h\nu)^{1/2}$ = zero on the hν axis, the optical band gap (E_{opt}) of the present transparent composite sample is determined to be 1.875 eV. The value of E_{opt} is influenced by the ratio of non-bridging oxygen (NBO's) to bridging oxygen in this material. NBO's are known to bind excited electrons less tightly than bridging oxygen, thus affecting the optical band gap [1, 47].

To further assess the degree of disorder within the present transparent composite sample, the Urbach energy (also known as the band tail, E_0) was determined. The E_0 of the present transparent composite sample was calculated by the following relation [48]:

$$\alpha(\nu) = B\exp[h\nu/E_0] \quad (3)$$

where B is a constant. Figure 14b shows the plot of ln α versus hν of the present transparent composite sample. The Urbach energy E_0 for the present transparent composite sample has been determined to be 1.038 eV. This value was calculated based on the reciprocal of the slope of linear portion observed in the ln α vs. hν plot. A high value of E_0 in this composite, suggests that weak bonds have been converted into defects within this material, emphasizing the presence

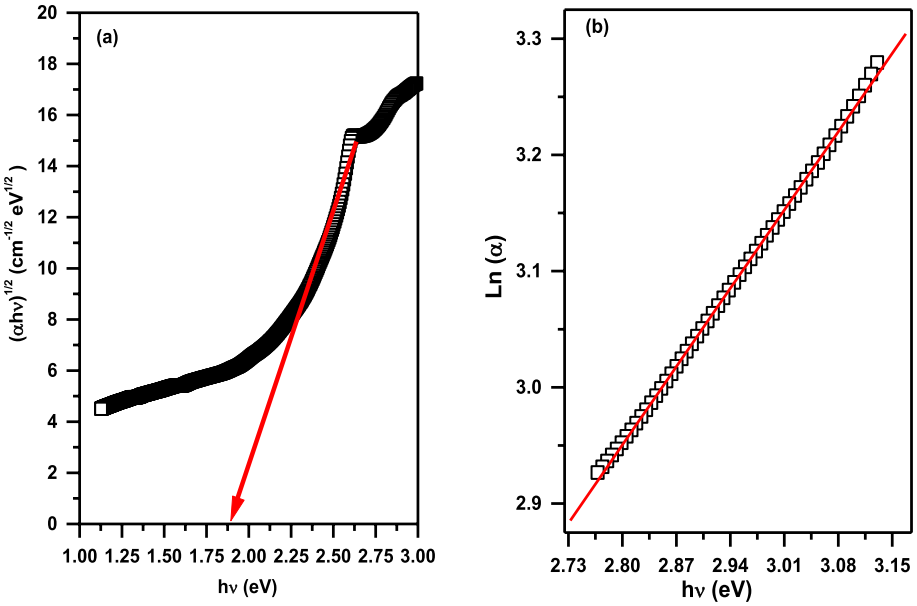

Fig. 14 **a** and **b** The plot of $(\alpha h\nu)^{1/2}$ versus $h\nu$ and the plot of ln α versus $h\nu$ of the present transparent composite sample, respectively

of structural disorder and defects that impact its properties [47].

Figure 15 displays the polarization versus electric field (P-E) of the present composite sample at various electric field. It is observed that the P-E loops at low electric field (10, 11, 13, and 14 kV/cm) exhibit double hysteresis loops, as well as an almost linear P-E relationship in the middle section of the hysteresis loop. The double hysteresis loops in the present composite sample could be explained by the presence of random local strain and defect dipoles in the ferroelectric of $BaTiO_3$ lattice [49–51]. Additionally, the other source of the double hysteresis loops in this sample is the first-order ferroelectric transition occurring in the temperature range between the Curie-Weiss temperature (T_0) and the Curie temperature (T_c) [52]. Therefore, in the first-order ferroelectric transition, double hysteresis loops are observed near T_c, indicating the electric field-induced phase transition from paraelectric to ferroelectric [50]. This finding is confirmed by the aforementioned dielectric results for the present composite sample, where the phase transition in this sample is of the first order. In ferroelectric material, the double hysteresis loops can be explained by the free energy perspective, where they can be induced by applying an external electric field under special conditions [52]. According to Pu et al., the double hysteresis loops in ferroelectric materials can be attributed to random local strain, which leads to the displacement of oxygen octahedra [51]. According to Randall et al., the double hysteresis loops in ferroelectric materials can be due to randomly oriented defect dipoles and/or switching of the first-order ferroelectric transition above T_c [52]. The reversible domain-switching mechanism in $BaTiO_3$ nanoparticles within the glass matrix may be driven by these point defects, which provide a restoring force and allow for substantial recoverable electrostrain [10]. The presence of random local strain and defect dipoles in $BaTiO_3$ nanoparticles via oxygen vacancy diffusion or oxygen octahedral rotations, as confirmed by the aforementioned HR-TEM and XPS results [10, 49]. Despite the double hysteresis loop (P-E) being an exceptional phenomenon in ferroelectric material, it is often observed in antiferroelectric materials [49]. But the presence of a double hysteresis loop (P-E) alone in any material does not provide evidence for the existence of antiferroelectric materials [52]. From the inset of Fig. 15 at 10 kV/cm, it is observed that the polarization is non-zero at zero electric field, thus the double hysteresis loop (P-E) in the present composite sample does not belong to the antiferroelectric type [53]. Therefore, we can conclude that the double hysteresis loop in the present composite sample at room temperature belongs to the ferroelectric type, which aligns with previous findings in $BaTiO_3$ reported by Merz [8]. Merz discovered for the first time the double hysteresis loop of ferroelectric $BaTiO_3$ at the Curie point [8]. Srivastava et al. studied the origin of the double hysteresis loops (P-E) in the ferroelectric $BaTiO_3$ crystal [54]. As the electric field is further increased (at 20, 25, 30, and 40 kV/cm), the hysteresis loops (P-E) narrow down and exhibit nearly linear dielectric behavior within these electric field ranges [15]. This suggests that the P-E loops transform from a double hysteresis loop to normal hysteresis loop with increasing electric field, possibly due to effects induced by the electric field near Curie temperature [10, 12]. This weakness of the double hysteresis loop and its transition to normal hysteresis loop with increased electric field corresponds with findings reported for $BiFeO_3$ ceramic by Yuan et al. [9]. The P-E loop of the transparent composite sample does not saturate (as seen in Fig. 7), which may be

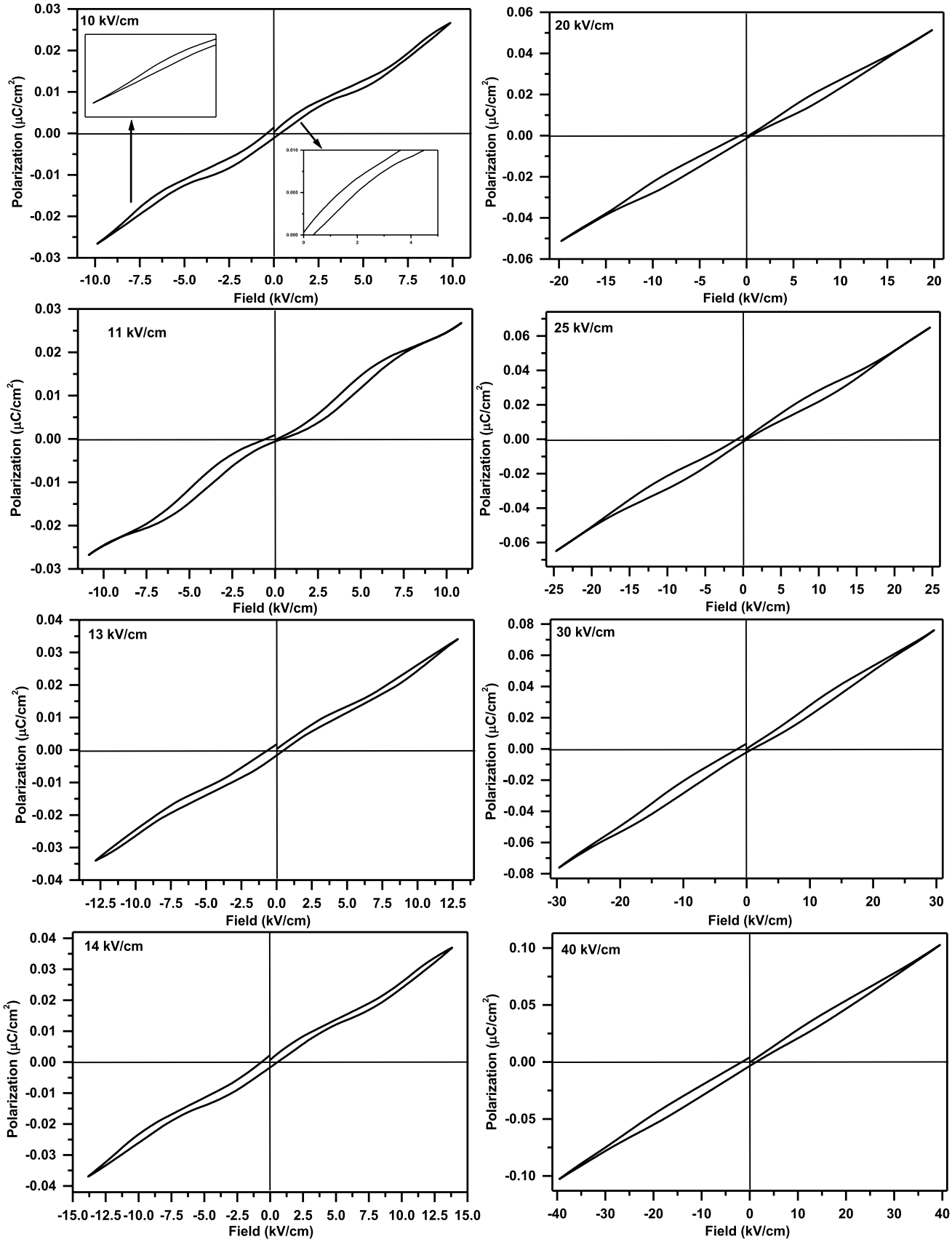

Fig. 15 The polarization versus electric field (P-E) of the present transparent composite sample at various electric field

Table 1 The hysteresis loops (P-E) parameters of the present glass-nanocomposite sample

Electric field (E) (kV/cm)	P_{max} ($\mu C/cm^2$)	P_r ($\mu C/cm^2$)	E_c (kV/cm)	A ($\mu C/cm^2 \cdot kV/cm$)
10	0.026	0.0011	6867.7	0.031
11	0.027	0.0006	7287.6	0.034
13	0.034	0.0016	10534.1	0.053
14	0.037	0.0017	11558.5	0.062
20	0.051	0.0013	12589.8	0.115
25	0.065	0.0014	13955.8	0.178
30	0.076	0.0022	25473.9	0.266
40	0.103	0.0035	28528.9	0.470

P_{max} is maximum polarization, P_r is remnant polarization, E_c is the coercive field, and A is loop area

attributed to three reasons: the electrical nonpolling of the glassy phase, the interface between the crystal ($BaTiO_3$) and glass, and the stresses applied on $BaTiO_3$ nanoparticles by the surrounding rigid glass matrix [55, 56]. Parameters of the P-E loops for the present transparent composite sample at various electric field are listed in Table1. It is noticed that the maximum polarization (P_{max}) increases with increasing the electric field, possibly due to the dielectric charging effect [57]. The lower values of remnant polarization (P_r) in the present transparent composite sample may be a result of the presence of the glassy phase and the smaller crystallite size of $BaTiO_3$ nanoparticles [56]. The values of the coercive field (E_c) and the loop area increase with increasing the electric field. A high E_c value in the present transparent composite sample can lead to electrical breakdown, thus preventing complete saturation [56]. The loop area of the P-E hysteresis loop represents the energy dissipated within the present composite sample. As the electric field increases, charge carriers within the $BaTiO_3$ move along the electric field, resulting in the dissipation of energy within this composite [58].>

4 Conclusions

In summary, we reported double hysteresis (P-E) loops for $BaTiO_3$ at room temperature in present transparent composite sample and explained the mechanisms of the double hysteresis loop (P-E) as exceptional phenomenon in the first order ferroelectric material. The transparent composite sample has been prepared by the melting quenching method. TEM, SAED, HR-TEM, and FTIR studies were employed to validate the existence of the $BaTiO_3$ nanoparticles within the borate glass matrix. XPS spectra provided evidence of the presence of oxygen vacancies, Ti^{3+} and Ti^{4+} ions in the present composite sample. DSC and dielectric studies of the present composite sample revealed the presence of a ferroelectric to paraelectric phase transition of $BaTiO_3$. Dielectric studies provided evidence that the phase transition in this sample is of the first order and the Curie-Weiss law was found to be valid at temperature above T_c. The optical characteristics of the present composite reveal the existence of octahedral transitions ($^2B_{2g} \rightarrow {}^2B_{1g}$ and $^2B_{2g} \rightarrow {}^2A_{1g}$) of Ti^{3+} ($3d^1$) ions in tetragonally distorted sites. The results obtained, such as double hysteresis (P-E) loops for $BaTiO_3$ in present transparent composite sample, can be used for the development of lead-free ferroelectric materials for energy storage applications.

Author contributions All listed authors have participated in the research presented in this paper.

Funding Open access funding provided by The Science, Technology & Innovation Funding Authority (STDF) in cooperation with The Egyptian Knowledge Bank (EKB).

Data availability All the data are available within this paper.

Declarations

Conflict of interest The authors declare that they have no conflict of interest.

Ethical statement This article does not contain any studies with human participants or animals performed by any of the authors.

References

1. E.K. Abdel-Khalek, E.A. Mohamed, S.M. Salem, F.M. Ebrahim, I. Kashif, Study of glass-nanocomposite and glass–ceramic containing ferroelectric phase. Mater. Chem. Phys. **133**, 69–77 (2012)
2. V. Thakur, A. Singh, R. Punia, M. Kaur, L. Singh, Effect of $BaTiO_3$ on the structural and optical properties of lithium borate glasses. Ceram. Int. **41**, 10957–10965 (2015)
3. E.K. Abdel-Khalek, I.O. Ali, Structural, AC conductivity and dielectric properties of vanado-tellurite glasses containing $BaTiO_3$. J. Non-Cryst Solids. **390**, 31–36 (2014)
4. L. Singh, V. Thakur, R. Punia, R.S. Kundu, A. Singh, Structural and optical properties of barium titanate modified bismuth borate glasses. Solid State Sci. **37**, 64–71 (2014)

5. J.H. Haeni, P. Irvin, W. Chang, R. Uecker, P. Reiche, Y.L. Li, S. Choudhury, W. Tian, M.E. Hawley, B. Craigo, A.K. Tagantsev, X.Q. Pan, S.K. Streiffer, L.Q. Chen, S.W. Kirchoefer, J. Levy, Schlom1. Nature **430**, 758 (2004)
6. E.K. Abdel-Khalek, E.A. Mohamed, I. Kashif, Ferroelectricity of strained $SrTiO_3$ in lithium tetraborate glass-nanocomposite and glass-ceramic. Phys. B **530**, 242–250 (2018)
7. C. Yuan, S. Ye, B. Xu, W. Lei, Strain induced tetragonal $SrTiO_3$ nanoparticles at room temperature. Appl. Phys. Lett. **101**, 071909 (2012)
8. W.J. Merz, Double Hysteresis Loop of $BaTiO_3$ at the Curie Point. Phys. Rev. **91**, 513–517 (1953)
9. G.L. Yuan, Y. Yang, S.W. Or, Aging-induced double ferroelectric hysteresis loops in $BiFeO_3$ multiferroic ceramic appl. Phys. Lett. **91**, 122907 (2007)
10. X. Ren, Large electric-field-induced strain in ferroelectric crystals by point-defect-mediated reversible domain switching. Nat. Mater. **3**, 91 (2004)
11. L.X. Zhang, X. Ren, In situ observation of reversible domain switching in aged Mn-doped $BaTiO_3$ single crystals. phys. Rev. B **71**, 17410 (2005)
12. L. Shebanov, M. Kusnetsov, A. Sternberg, Electric field-induced antiferroelectric-to-ferroelectric phase transition in lead zlrconate titanate stannate ceramics modified with lanthanum. J. Appl. Phys. **76**(7), 4301–4304 (1994)
13. N. Chopra, S. Kaur, O.P. Pandey, G. Sharma, S. Sharma, Physical, optical and structural characterizations of Dy^{3+}-doped lead borate glasses, IOP Conf. Series: Materials Science and Engineering 1114 (2021) 012098
14. E.K. Abdel-Khalek, E.A. Mohamed, S.M. Salem, I. Kashif, Structural and dielectric properties of $(100-x)B_2O_3$-$(x/2)Bi_2O_3$–$(x/2)Fe_2O_3$ glasses and glass-ceramic containing BiFeO3 phase. J. Non-Cryst Solids. **492**, 41–49 (2018)
15. X. Tan, Z. Xu, X. Liu, Z. Fan, Double hysteresis loops at room temperature in $NaNbO_3$-based lead-free antiferroelectric ceramics. Mater. Res. Lett. **6**, 159–164 (2018)
16. E.K. Abdel-Khalek, E.A. Mohamed, Shaaban M. Salem, Dielectric and Pyroelectric properties of $BaTiO_3$ embedded in $Li_2B_4O_7$ Glass Matrix, Ferroelectrics, **473** (2014) 34–44
17. G. Senthil Murugan, K.B.R. Varma, Lithium borate–strontium bismuth tantalate glass nanocomposite: a novel material for nonlinear optic and ferroelectric applications. J. Mater. Chem. **12**, 1426–1436 (2002)
18. N. Syam Prasad, K.B.R. Varma, Evolution of ferroelectric $LiNbO_3$ phase in a reactive glass matrix ($LiBO_2$–Nb_2O_5), J. Non-crys. Solids. **351**, 1455–1465 (2005)
19. C. Liu, S. Xie, H. Bai, F. Yan, T. Fu, B. Shen, Jiwei Zhai excellent energy storage performance of niobate-based glass-ceramics via introduction of nucleating agent. J. Materiomics. **8**, 763–771 (2022)
20. Y. Hao, Z. Feng, S. Banerjee, X. Wang, S.J.L. Billinge, J. Wang, K. Jin, K. Bi, L. Li, Ferroelectric state and polarization switching behaviour of ultrafine $BaTiO_3$ nanoparticles with large-scale size uniformity. J. Mater. Chem. C **9**, 5267 (2021)
21. L. Zhao, D. Guo, X. Kang, L. Liang, Z. Yang, Y. Sang, H. Liu, Morphology tuned $BaTiO_3$ ceramic sintering: crystal facet and size distribution. Sci. Adv. Mater. **8**, 1200–1207 (2016)
22. K. Gupta, S. Singh, M. Ceretti, M.S.R. Rao, W. Paulus, Scaling of extended defects in nano-sized brownmillerite $CaFeO_{2\cdot5}$, Phys. Status Solidi A **210**, 1771–1777 (2013)
23. E.K. Abdel-Khalek, E.A. Mohamed, A. Ratep, S.M. Salem, I. Kashif, Structural, optical and dielectric characterization of niobium lithium tetraborate glasses doped praseodymium. J. Non-Cryst Solids. **441**, 58–65 (2016)
24. D.D. Ramteke, H.C. Swart, R.S. Gedam, Spectroscopic properties of Pr^{3+} ions embedded in lithium borate glasses. Phys. B **480**, 111–115 (2016)
25. T.S. Rao, N.V. Prasad, M. Shareefuddin, G. Prasad, Indian J. Sci. Technol. **15**(17), 839–849 (2022)
26. E.K. Abdel-Khalek, S.M. Salem, M. Farouk, E.A. Mohamed, I. Kashif, Structural, optical and dielectric properties of glass-nanocomposite. J. Non-Cryst Solids. **357**, 864–872 (2011)
27. C. Gautam, A.K. Yadav, A.K. Singh, A review on Infrared Spectroscopy of Borate glasses with effects of different additives ISRN ceramics. ID **428497**, 17 (2012)
28. I. Ardelean, P. Pascuta, Comparative vibrational study of $xFe_2O_3\cdot(1-x)[3B_2O_3\cdot MO]$ (MO⇒CaO or CaF_2) glass systems. Mater. Lett. **58**, 3499 (2004)
29. K. Swapna, A. Mahamuda, S. Srinivasa Rao, T. Shakya, D. Sasikala, G. Haranath, Vijaya, Prakash, Spectrochim. Acta Part A Mol. Biomol. Spectrosc. **125**, 53–60 (2014)
30. S. Thakur, V. Thakur, A. Kaur, L. Singh, Study of the crystallization and structural behavior of Bismuth Barium Titanate Glass-ceramics. J. Non-Cryst Solids. **557**, 120563 (2021)
31. N.R. Lakshmi, S. Cole, Influence of TiO_2 ions on Spectroscopic Properties of Oxyfluoride Glasses, Materials Today: Proceedings 18 (2019) 192–206
32. D.A. Hensley, S.H. Garofalini, XPS investigation of lithium borate glass and the $Li/LiBO_2$, Interface. Appl. Surf. Sci. **81**, 331–339 (1994)
33. K.M. Kaky, E. Şakar, U. Akbaba, A.E. Kasapoğlu, M.I. Sayyed, E. Gür, S.O. Baki, M.A. Mahdi, X-ray photoelectron spectroscopy (XPS) and gamma-ray shielding investigation of borosilicate glasses contained alkali/alkaline modifier. Results Phys. **14**, 102438 (2019)
34. R. Harizanova, M. Pernikov, I. Mihailova, D. Tatchev, G. Avdeev, I. Avramova, C. Rüssel, J. Chem. Technol. Metall. **58**, 8–13 (2023)
35. Y. Gong, W. Deng, W. Zhang, C. Yatongchai, Y. Zou, R.C. Buchanan, Effect of a BaO-CuO-Bi_2O_3-B_2O_3 glass flux, and its processing on the dielectric properties of $BaTiO_3$ Ceramics International 41 (2015) 671–680
36. E.K. Abdel-Khalek, A.A. Askar, M.A. Motawea, M.A. Aboelnasr, H.H. El-Bahnasawy, Study of the influence of synthesis method in $BaFeO_{3-\delta}$ perovskite on structural, optical, magnetic and antibacterial properties. Phys. B: Phys. Condens. Matter. **628**, 413573 (2022)
37. L. Srisombat, S. Ananta, B. Singhana, T.R. Lee, R. Yimnirun, Chemical investigation of Fe^{3+}/Nb^{5+}-doped barium titanate ceramics. Ceram. Int. **39**, S591–S594 (2013)
38. M. Wegmann, L. Watson, A. Hendry, XPS Analysis of submicrometer barium titanate powder. J. Am. Ceram. Soc. **87**, 371–377 (2004). [3]
39. C. Miot, E. Husson, C. Proust, R. Erre, Coutures X-ray photoelectron spectroscopy characterization of barium titanate ceramics prepared by the citric route. Residual carbon study. J. Mater. Res. **12**, 2388–2392 (1997)
40. V.U. Rahangdale, V.K. Deshpande, Study of physical properties of $PbTiO_3$ based glass-ceramic with variation of heat treatment duration. Ferroelectrics. **467**, 85–98 (2014)
41. E.K. Abdel-Khalek, M.A. Elsharkawy, M.A. Motawea, E. Elesh, A.T.M. Farag, Dielectric and Thermal properties of Tetragonal $PbTiO_3$ Nanoparticles/Clusters embedded in Lithium Tetraborate Glass Matrix. Silicon. **13**, 2993–3002 (2021)
42. C.J. Xiao, C.Q. Jin, X.H. Wang, Crystal structure of dense nanocrystalline $BaTiO_3$ ceramics. Mater. Chem. Phys. **111**, 209 (2008)
43. E.A. Mohamed, E. Nabhan, A. Ratep, F.M. Hassan, K. Tahoon, Influence of $BaTiO_3$ nanoparticles/clusters on the structural and

dielectric properties of glasses nanocomposites. Phys. B **589**, 412220 (2020)
44. E.K. Abdel-Khalek, S.M. Salem, I. Kashif, Synthesis, crystal structure and ferroelectric properties of $SrBi_2Nb_2O_9$ embedded in a 50% $Li_2B_4O_7$ glass matrix. J. Electroceram. **29**, 171–178 (2012)
45. P. Nageswara Rao, C. Laxmi Kanth, D. Krishna Rao, N. Veeraiah, J. Quant. Spectrosc. Radiat. Transf. **95**, 373 (2005)
46. N.F. Mott, E.A. Davis, *Electronic Processes in Non-Crystalline Materials*, 2nd edn. (Clarendon, Oxford, 1979)
47. E.K. Abdel-Khalek, A.A. Bahgat, Optical and dielectric properties of transparent glasses and nanocrystals of lithium niobate and lithium diborate in borate glasses. Phys. B **405**, 1986–1992 (2010)
48. F. Urbach, The long-wavelength edge of photographic sensitivity and of the electronic absorption of solids. Phys. Rev. **92**, 1324 (1953)
49. Y. Pu, J. Zhu, X. Zhu, Y. Luo, M. Wang, X. Li, J. Liu, J. Zhu, Xiao. Double hysteresis loop induced by defect dipoles in ferroelectric $pb(Zr_{0.8}Ti_{0.2})O_3$ thin films. J. Appl. Phys. **109**, 044102 (2011)
50. K. Li, X.L. Zhu, X.Q. Liu, X. Ma, M.S. Fu, J. Kroupa, S. Kamba, X.M. Chen, Electric-field-induced phase transition and pinched P–E hysteresis loops in Pb-free, ferroelectrics with a tungsten bronze structure. NPG Asia Mater. **10**, 71–81 (2018)
51. Y. Pu, D. Liu, X. Shi, Double-hysteresis-like loops in $Cr_2Ti_3O_9$-doped $BaTiO_3$ ceramics. Vacuum. **99**, 38–41 (2014)
52. C.A. Randall, Z. Fan, I. Reaney, L.-Q. Chen, S.T. McKinstry, Antiferroelectrics: history, fundamentals, crystal chemistry, crystal structures, size effects, and applications. J. Am. Ceram. Soc. **104**, 3775–3810 (2021)
53. K. Banerjee, S. Asthana, Scaling behavior of different shapes of hysteresis loops and recoverable energy storage density in Na0.5Bi0.5TiO3, K0.5Bi0.5TiO3, and Na0.25K0.25Bi0.5TiO3 ferroelectrics. J. Materiomics. **8**, 918–927 (2022)
54. N. Srivastava, G.J. Weng, A theory of double hysteresis for ferroelectric crystals. J. Appl. Phys. **99**, 054103–054111 (2006)
55. V.U. Rahangdale, D.K. Gala, R.M. Acharya, V.K. Deshpande, Dielectric and ferroelectric properties of Al_2O_3 containing lead titanate based glass-ceramics, AIP Conf. Proc. 1591 (2014) 705–707
56. J. Shankar, G.N. Rani, J. Anjaiah, P. Raju, V.K. Deshpande, Study of Microstructure and Dielectric Properties of $PbTiO_3$ based Glass Ceramics, AIP Conference Proceedings 2162 (2019) 020045-6
57. H. Qiao, C. He, Z. Wang, D. Pang, X. Li, Y. Liu, X. Long, Influence of Mn dopants on the electrical properties of $pb(In_{0.5}Nb_{0.5})O_3$-$PbTiO_3$ ferroelectric single crystals. RSC Adv. **7**, 32607–32612 (2017)
58. H.-I. Hsiang, K.-Y. Lin, F.-S. Yen, C.-Y. Hwang, Effects of particle size of $BaTiO_3$ powder on the dielectric properties of $BaTiO_3$/polyvinylidene fluoride composites. J. Mater. Sci. **36**, 3809–3815 (2001)